communications engineering

A Nature Portfolio journal

Article

https://doi.org/10.1038/s44172-025-00516-0

Adaptive continuous-shape-changing solar-powered microfliers enabled by a drone-mounted releasing module

Check for updates

Haoyang Sun[1], Chenxi Yang[1], Zhenlong Wang[1], Yifan Wang[1], Xinrui Zhang[1], Yunhao Ren[1], Wenhua Li[1], Honglong Chang[1], Kan Li[2], YongAn Huang[2], Binghe Ma[1], Weizheng Yuan[1] & Tao Ye[1]

The exceptional adaptability of biological organisms to new environments is difficult to replicate in artificial robots. Although dandelion-inspired microfliers have successfully mimicked passive wind dispersal of dandelion seeds with long travel distances and certain controllable landing capacities, existing designs have yet to replicate the adaptive abscission and continuous-shape-changing mechanisms observed in species. Here we propose a programmable adaptive continuous-shape-changing solar-powered microflier enabled by a drone-mounted releasing module and actuated by the shape memory alloy actuators with a minimal total weight of 198 mg. The designed microfliers synergistically mimic the adaptive abscission and continuous-shape-changing mechanisms of dandelion seeds, enabling swarm adjustments of aerodynamics and flight performances in response to multi-environmental factors. Moreover, our microfliers demonstrate controlled interval deployments, programmable flight performances, and robust self-sustaining operations, facilitating their level of intelligence and practical applications.

In recent years, intelligent robots have been developed by systematically emulating the structural and functional characteristics of organisms[1–5], which are accumulated through multimillion-year evolutionary processes. However, the exceptional adaptability of biological organisms to new environments is difficult to replicate in robots[6]. As a representative example, dandelion capitulum controls the developing, ripening, and adaptive abscission of seeds with continuous-shape-changing aerodynamic pappus[7–9], leading to adaptive adjustments of dispersal path and landing points[10,11] of seeds to reach the high-humidity environment suitable for germination[12,13]. Although the drag-enhancing configuration of compositae seeds (including dandelion and tragopogon pratensis, etc.) has been partially implemented in artificial microflier systems[14–17], existing designs failed to mimic the adaptive abscission and continuous-shape-changing processes in natural dandelions or other compositae families, resulting in limited aerodynamic control capability and poor flight performance.

The initial systematic adoption of dandelion seed flight characteristics was realized through the battery-free wireless sensing devices[14], which have been demonstrated to enable backscatter communication, wide-area dispersal, and upright landing with certain aerodynamic stability. However, the falling behaviors of these devices are random and lack active control ability. To endow microfliers with active control capability, researchers further proposed the solar-powered binary-state origami microfliers[18] that allowed for flight trajectory switching between tumbling and stable states through remotely triggered electromagnetic actuation, thereby varying the travel distances in mid-air. This study did not replicate the continuous-shape-changing aerodynamic structure of the dandelion, and the binary-state origami design incurred additional weight, restricted post-landing solar energy harvesting angles, and limited control capacity. Upon attaining a comprehension of dispersal mechanisms inherent in dandelion seeds, researchers designed the light-driven dandelion-inspired aerodynamic structure without any electronic components integration[15], the deformation degrees of the "pappus" could be controlled by changing the light irradiations. However, the light-driven structure suffered from limited in-device flight control capability and a deficiency of electrical functionalities due to the lack of electronic components. Thus, while the current artificial aerodynamic structures or microfliers demonstrated certain drag-enhancing performance and flight control capacity, the previous studies have not systematically investigated the adaptive abscission and continuous-shape-changing dispersal mechanisms within dandelion-inspired microfliers, and the abscission of dandelion seeds from the capitulum was a prerequisite for natural dispersal[9], as this process regulated the timing of seed dispersal and contributed to aerodynamic morphological development of seeds[19].

[1]Ministry of Education Key Laboratory of Micro/Nano Systems for Aerospace, Key Laboratory of Micro- and Nano-Electro-Mechanical Systems of Shaanxi Province, School of Mechanical Engineering, Northwestern Polytechnical University, Xi'an, China. [2]State Key Laboratory of Manufacturing Equipment and Technology, Flexible Electronics Research Center, Huazhong University of Science and Technology, Wuhan, China. e-mail: yetao@nwpu.edu.cn

Here, we develop adaptive continuous-shape-changing solar-powered microfliers enabled by a drone-mounted releasing module by mimicking the adaptive abscission and continuous-shape-changing dispersal mechanisms of compositae seeds, and further enhance adaptability from a single-environmental factor to multi-environmental factors. The proposed adaptive continuous-shape-changing ability is derived from the co-actuation of a drone-mounted releasing module, called the environment adaptive module (EAM), and the shape memory alloy actuator (SMAA). Programmable aerodynamic controls of microfliers are achieved through continuous-shape-changing strategies of two basic shapes (saddle and hemisphere), resulting in swarm adjustments of flight behaviors (e.g., flight trajectories, rotational speeds, travel distances, and landing points). A on-chip heterogeneous integration strategy is proposed to maintain the designed aerodynamic structure during the falling process, and robust self-sustained operation is achieved through harvesting environmental solar energy.

Results

Adaptive design of bioinspired microfliers

Inspired by the wind dispersal mechanisms of dandelion seeds, we developed adaptive continuous-shape-changing solar-powered microfliers. Figure 1a provides a comparison between the adaptive shape-changing mechanisms of dandelion seeds and the proposed microfliers. While dandelion seeds only adapt to changes in humidity[10], the aerodynamic shapes of proposed microfliers can adaptively change to various environmental factors (e.g., temperature, light, and humidity). The shape memory alloys (SMAs) are widely used smart materials with unique properties, such as lightweight, fast actuation speed, and continuous actuation force[20,21]. We adopted the shape memory effect of SMAs to enable adaptive continuous-shape-changing in microfliers, resulting in programmable aerodynamic controls. The microflier integrated with the one-way SMA wires could continuously change from its preset state to any desired angle and return to its original preset state upon heating (Fig. 1b). The SMA wires were prepared as SMA actuator (SMAA) according to the integration requirements (see the "Methods" section for details). Similar to the continuous-shape-changing process of tragopogon seeds, which shared the same pappus morphology as dandelions and exhibited a size even closer to our designed structure, the developed microfliers achieved free-space continuous-shape-changing (from flat to different angles) when actuated by the SMAAs, demonstrating the effectiveness of the SMAAs in driving controlled actuation (Fig. 1c and Supplementary Fig. 1).

The overall structure of the proposed microflier consists of two core layers (biomimetic aerodynamic layer and flexible circuit layer with solar power management and multi-parameter sensing circuits), SMAA unit, and two solar cells, as shown in Fig. 1d (detailed preparation methods are provided in the "Methods" section). This design eliminated the complex external wiring, allowing the microfliers to reduce weight and demonstrate optimal dispersal performance. To further minimize the weight of the microflier, we separated the adaptivity module from the microflier, the EAM, similarly functioning to the "capitulum" was mounted on a minidrone, and the microflier similarly functioning to the wind-dispersed tragopogon seeds (Fig. 1e).

The microfliers can be delivered through a minidrone to the target environments, and the shape and release timing of the microfliers were controlled by the EAM, which can make adaptive decision-driven SMAA shape-changing. This shape-changing response was automatically triggered by the embedded program of EAM. When the sensed data exceeded the preset threshold (such as temperature, pressure), the microcontroller unit (MCU) activated the delay, providing power to drive the SMAA deformation. Before deployment, the EAM senses to multi-environmental factors and outputs electricity to SMAA to control adaptive shape-changing of microfliers, enabling flight performance adjustments for landing on demand (Supplementary Fig. 2). The microfliers, integrated with multi-functional circuits and solar cells, achieve self-sustained operation by harvesting environmental solar energy, which enables effective detection of potential environmental hazards and continuous monitoring after deployment. The designed microfliers enhance the intelligence level of unmanned devices with potential applications in autonomous environmental monitoring, site-specific landing, and self-sustained operation across diverse terrains.

The continuous-shape-changing mechanisms

The shape-changing behaviors of the microfliers alter the projected areas of biomimetic pappus structures along different axes[14], influencing their terminal velocities and dispersal performances under crosswinds. This study employed finite element simulation to model the internal stress distribution of flat, saddle, and hemisphere aerodynamic shapes with different angles in the longitudinal and lateral wind fields (Fig. 2a, b, see Methods section for details). The arc-shape aerodynamic structure in Fig. 2a (curvature $\rho \approx 0.042\ \mathrm{mm}^{-1}$), which is based on the curvature of the samara seed edge and aligned more closely with the natural configuration of dandelions, exhibits a non-uniform stress distribution resembling the self-rotating tendency[22,23]. However, the stress field distribution of straight-shape (str-shape) aerodynamic structure was evenly distributed (Supplementary Fig. 3), which was not conducive to self-rotation. The experimental results showed that the arc-shaped aerodynamic structure has a longer travel distance than the straight-shaped aerodynamic structure (Supplementary Fig. 4), which was in agreement with the simulation results.

Simulation models (Fig. 2b) were built based on the aerodynamic complexity from one degree of freedom (saddle) to multi-degree of freedom (hemisphere). Simulation results revealed that the two different aerodynamic structures with the same shape-changing angle (θ) of 20° experienced different wind-facing stress distributions (Fig. 2c). This phenomenon suggested that microfilers with different shapes exhibited distinct flight behaviors during descent. We placed the two aerodynamic shapes in rotating lateral wind fields with an airflow speed of 1 m s^{-1} to simulate the force they experienced (Fig. 2d). The stress on the saddle aerodynamic structure exhibited sinusoidal distribution across different directions (minimum at 0° and 180°, maximum at 90°), while the hemisphere aerodynamic structure demonstrated relatively stable stresses in all directions. It is generally assumed that a more stable force distribution (hemisphere) led to better (stable) flight performance. However, the unpredictable flight trajectories of saddle aerodynamic structure caused by uneven force distribution might enable other interesting applications, e.g., antipredator defense motion of many organisms[24]. Furthermore, to demonstrate the effectiveness of the designed pattern structures in regulating the flow fields, we simulated the flow fields under two typical wind directions (vertical and crosswind). The results indicated that patternless structures and drag-enhanced patterned structures all exhibited separated vortex rings in two conditions (simulation details can be found in the "Methods" section), which confirmed that characteristic features like the separated ring vortex, observed in natural dandelions, also appeared in the proposed artificial system (Supplementary Fig. 5).

While the two designed aerodynamic structures exhibited distinct shape-changing performances in simulations, implementing adaptive continuous shape-changing in the proposed microfliers remained a major challenge. Considering the programming complexity and power consumption of shape-changing for microfliers, we selected the one-way SMA wires with a 0.3 mm diameter to deliver just enough actuation force for reliable continuous-shape-changing while minimizing detrimental weight penalties to dispersion performance (the selection analysis of SMA is detailed in Supplementary Table 1 and Supplementary Note 1). While larger diameter SMA wires can increase actuation force and contraction speed, excessive mass may induce a sharp rise in terminal velocity. This will lead to the failure of long-distance wind dispersion. Figure 2e illustrates the continuous shape-changing of a microflier driven by a SMAA, and the cross-sectional diagram shows how the SMAA continuously changes the shape of the microflier from a specific angle (θ) to a flat state, and the detailed mechanism analysis can be found in Supplementary Note 1. Temperature is a important bridge between the electricity flows and the kinematic states of

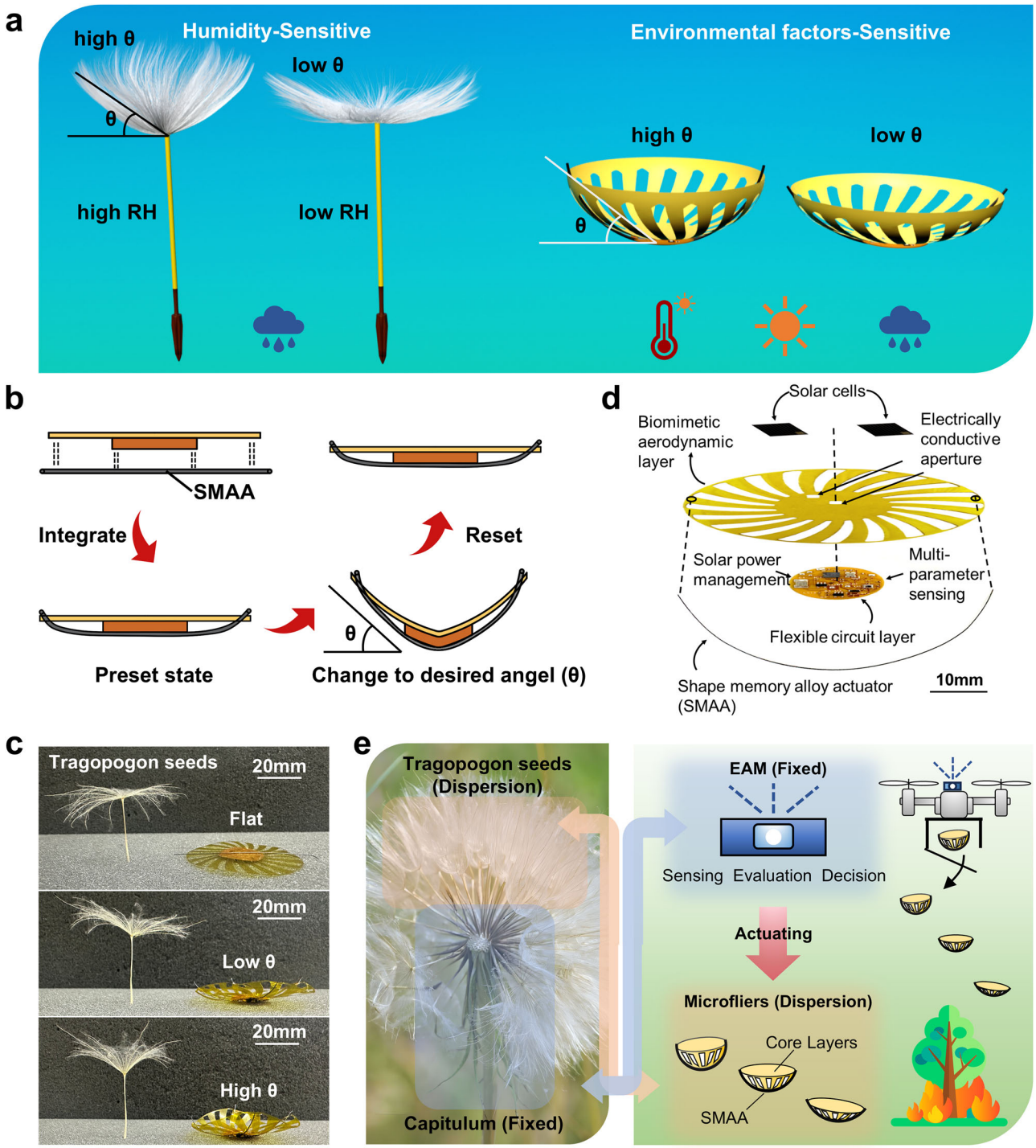


Fig. 1 | Adaptive continuous-shape-changing solar-powered microfliers enabled by a drone-mounted releasing module. a Schematics of the shape-changing mode of the proposed microflier, which simulates the shape-changing mechanism of a dandelion seed. The angle (θ) of the dandelion seeds is mainly influenced by the relative humidity (RH). **b** Diagrams show the shape-changing process of a microflier with the assistance of a shape memory alloy actuator (SMAA). **c** Tragopogon pratensis seed (left) demonstrating a multi-angle umbrella-shaped aerodynamic structure, and the microflier (right) is actuated by SMAAs in different shapes. **d** Disassembled view of the adaptive continuous-shape-changing solar-powered microflier with major components. **e** Schematics of the microfliers' integration and function strategy. The interaction of the microfliers and the environment adaptive module (EAM) mimics the adaptive abscission and continuous-shape-changing dispersal mechanisms between the tragopogon seeds and capitulum.

SMAs[25]. Once the type and size of SMAs are selected, the shape-changing angle of the SMAA can be controlled by programming the current (I) or the start-up times (t) according to Joule's law[26,27]. We adopted a 50 mm diameter arc-shape structure as the biomimetic aerodynamic layer and the experimental results demonstrated that this structure not only possessed a high load capacity (V_t of ~1.638 m s^{-1} with 159.7 mg, Supplementary Fig. 6), but also met the target mass and providing ample space (diameter of 20 mm) for the integration of subsequent electronic components (Supplementary Fig. 7).

We mounted the SMAAs onto the biomimetic aerodynamic layers using cyanoacrylate adhesive (CA) glue through a heterogeneous integration approach, and the biomimetic aerodynamic layers could be deformed

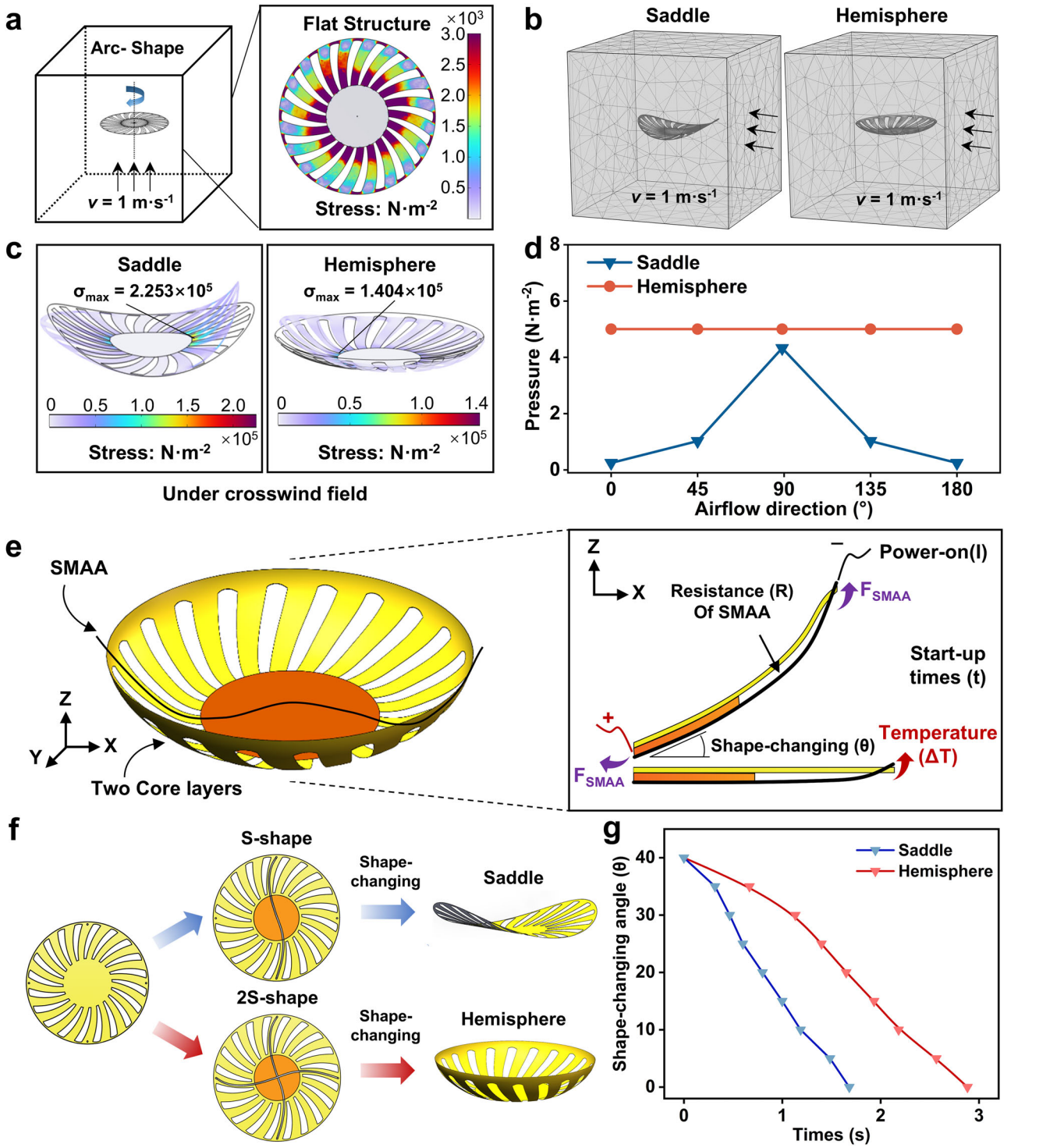


Fig. 2 | The continuous-shape-changing mechanisms. a The simulated stress field distribution of the flat aerodynamic structure under longitudinal wind field. **b** Simulation models of saddle and hemisphere aerodynamic structures under crosswind fields. **c** The simulated stress field distributions of the saddle and hemisphere aerodynamic structures under crosswind fields. **d** Stress variations of saddle and hemisphere aerodynamic structures under rotational crosswind fields. **e** The schematic shows continuous-shape-changing of aerodynamic structure enabled by shape memory alloy actuator (SMAA). **f** Formation schematics of the saddle and hemisphere aerodynamic structures with 2 distinct SMAAs integration strategies (S and 2S-shape). **g** The specific variations of angle (from 40° to 0°) over shape-changing time for saddle and hemisphere microfliers.

into saddle and hemisphere structures based on different integration strategies: S-shape and 2S-shape (Fig. 2f). The saddle (S-shape) and hemisphere (2S-shape) structures offered multiple real-time control modes for the microfliers with programmable aerodynamics. We qualitatively plotted the curves of the shape-changing angles of the two aerodynamic structures with a micro-lithium battery (3.7 V) power supply, concerning their actuating effects on the microfliers (Fig. 2g). The results showed that the saddle aerodynamic structure could reduce the angle from 40° to 0° within 1.68 s and the hemisphere aerodynamic structure could reduce angle from 40° to 0° within 2.88 s. These results indicated that SMAAs could precisely control the continuous-shape-changing of microfliers, breaking through the limitations of binary-state shape-changing[18].

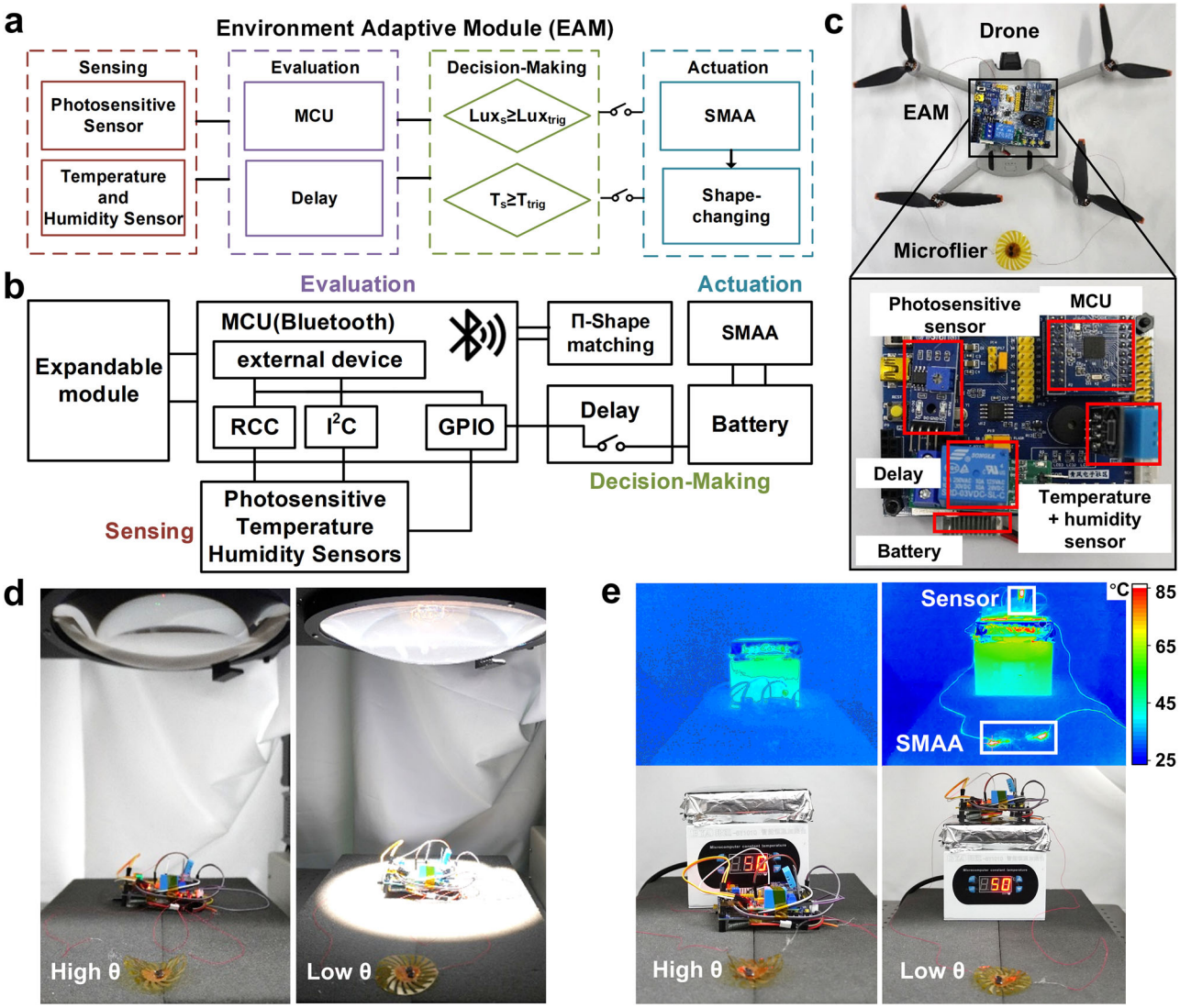


Fig. 3 | The adaptive continuous-shape-changing mechanisms. a Flowchart illustrates the operation process of the environment adaptive module (EAM) to drive the adaptive continuous-shape-changing of the microflier through shape memory alloy actuators (SMAAs). **b** Circuit diagram of EMA, including sensing, evaluation, decision-making, continuous-shape-changing, and expandable modules. **c** The photograph of the drone, EMA, and microflier. Five specific modules are integrated within the EMA. **d**, **e** The adaptive continuous-shape-changing of the microflier (from high θ to low θ) as a response to simulated light intensity and temperature.

The adaptive mechanisms and aerodynamic adjustments

The primary challenge in achieving adaptive continuous-shape-changing for microfliers is the high power consumption and additional weight of the actuator system. Unlike natural systems, artificial microfliers face energy constraints at a limited scale. Although the microfliers can sense changes in environmental humidity, they lack sufficient energy to drive their large continuous deformation in this study. To address this issue, we designed the EAM module to conduct environmental sensing, evaluation, and decision-making tasks (Fig. 3a, b). The microfliers and external multifunctional module, called EAM, would cooperatively operate with the SMAAs to control the continuous-shape-changing (Fig. 3c, "Methods" section). The MCU module regulated the switching operations of the delay module (controlled the precise electricity power flowed through the SMAA) through real-time analysis of multi-environmental parameters acquired from the multi-parameter sensors. The power supply channels of the delay module and SMAA were interconnected through ~0.13 mm diameter wires. Through the synergistic EAM-SMAA actuating system to mimic morphological development and the abscission of dandelion seeds from the capitulum, the microflier achieved adaptive continuous-shape-changing and controllable release (Supplementary Note 2). Furthermore, to demonstrate the microflier's adaptive continuous-shape-changing capability, we conducted experiments under various light and temperature conditions (Fig. 3d, e, "Methods" section). The results indicated that when the EAM module detected sudden changes in light or temperature, it could accurately trigger the adaptive continuous-shape-changing of the microflier (Supplementary Movies 1 and 2).

Shape analyses of the microfliers revealed that the shape-changing angle (θ) was the key factor influencing lateral displacement capability. We conducted the study on the shape-changing angle of its two main influencing aspects: terminal speed and lateral displacement capability. Firstly, we tested and recorded their terminal velocities in Supplementary Fig. 8a, b. The results showed that the average terminal velocity (ATV) of the saddle microflier significantly lower than hemisphere at the same angle (e.g., ATV of 10° saddle was 1.54 m s^{-1} and ATV of 10° hemisphere was 1.66 m s^{-1}), while the ATV of the only payload without any artificial aerodynamic structure was 4.60 m s^{-1} ($N = 5$, error bars = ±σ). The saddle or hemisphere microflier can disperse hundreds of meters (≥61 m) in the same conditions, while the payload was able to disperse only a few meters (≤10 m) due to its excessively rapid descent terminal velocity (Supplementary Fig. 8c, d). Secondly, to study the effect of different shape-changing angles on lateral

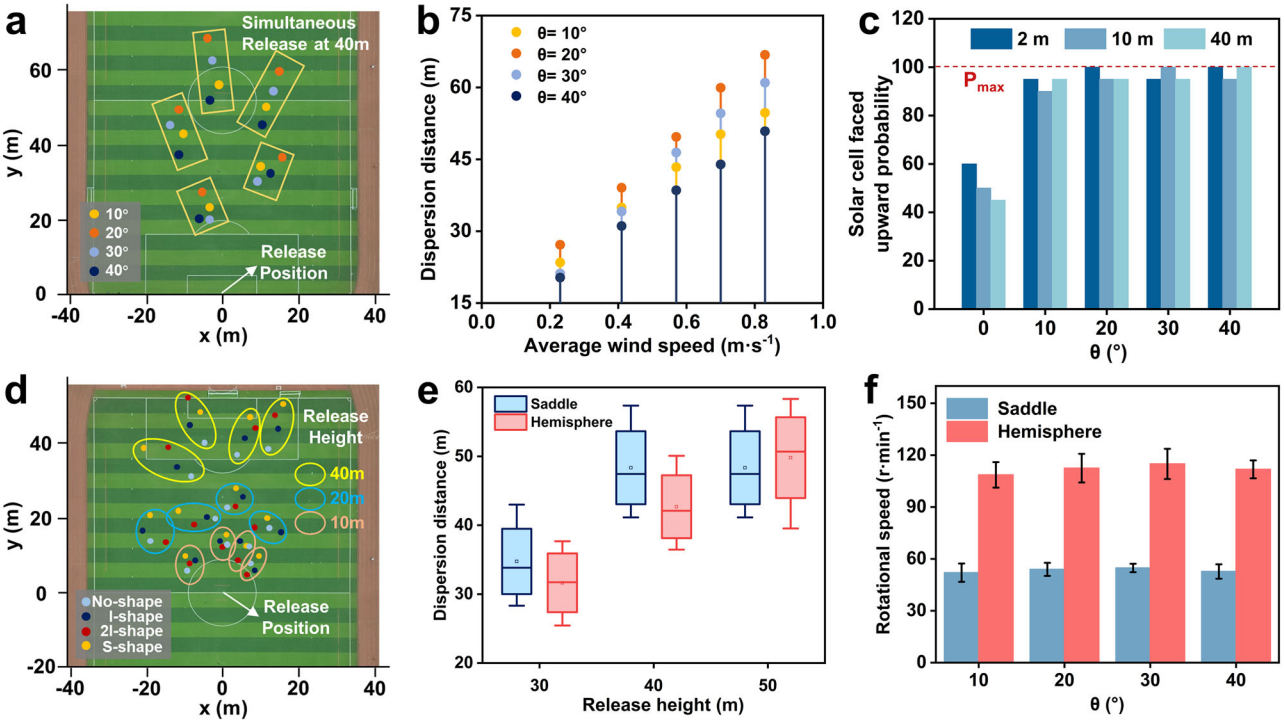


Fig. 4 | The aerodynamic adjustments of microfliers. a, **b** Diagrams show the microfliers' landing locations, where the drone simultaneously releases saddle microfliers at different shape-changing angles from a height of 40 m. The microfliers exhibit controllable intervals under different wind speeds. **c** The correlation between the probability of solar cells faced upward and the shape-changing angle of saddle microfliers at 2 m-indoor, 10 m-outdoor, and 40 m-outdoor release heights ($N = 20$ trials). **d** Outdoor drop experiments from 10 m, 20 m, and 40 m for 3 different types of microfliers ($N = 4$ trials). **e** The box plot shows the dispersal performances of saddle and hemisphere microfliers, which are released simultaneously at different heights (30 m, 40 m, 50 m). **f** Diagram shows the rotational speeds of the saddle and hemisphere microfliers with four different shape-changing angles (Error bars show standard deviation calculated from $N = 5$ independent trials).

displacement capability, we used the saddle microflier as the experimental object (see "Methods" section for details). The results showed that under different average wind speeds, the microfliers with an angle of 20° achieved the longest dispersal distance, although their terminal speeds are not as low as 10° (Fig. 4a, b). It indicated that at 20°, the best dispersion distance performance was achieved due to the combined influence of two factors (the terminal speed and lateral displacement capability).

During the experiments shown in Fig. 4a, b, we deliberately choose to release the microfliers when the wind direction is roughly towards the landing point along the *y*-axis direction. The four different angles microfliers were released simultaneously, so we further observed that the microfliers could achieve regularly spaced distributions under suitable wind conditions (varying details of wind speed are in Supplementary Fig. 9), demonstrating the ability to adjust the performance of microflier deployments. Furthermore, to measure the optimal travel distances of microfliers, we dropped the saddle microfliers with an angle of 20° at different heights, dispersing approximately 104 m distance at 40 m height (Supplementary Fig. 10 and Supplementary Movie 3), which indicated a record travel distance/height value of 2.6 (wind speed of ~2.38 m s^{-1}) for microlfiers with active shape-control capability[18]. In addition, Fig. 4c ($N \geq 20$) showed that the microfliers integrated with SMAAs achieved a significantly higher solar cells faced upward probability of above 90%, despite being affected by the airflow from the minidrone in the outdoor environments, as compared to non-SMAA microfliers (only 45% to 60%). The wind speed of the experiment on that day was recorded in Supplementary Fig. 11, which was one of the core factors influencing the probability of landing. The stronger posture adjustment ability (solar cells faced upward) was a prerequisite for maximum harvesting of the environmental solar energy and supporting the normal operation of multi-sensing and communication modules within the microfliers.

The proposed saddle and hemisphere microflier structures might exhibit distinct flight performances. We introduced the saddle and hemisphere microfliers with a fixed shape-changing angle (20°) for the dispersal experiments, and the non-SMAA microfliers were used for comparison. Dispersal experiments were conducted with release heights at 10 m, 20 m, and 40 m, landing positions were recorded to analyze the flight performances of these microfliers (Fig. 4d). The results showed that at 10 m and 20 m, the saddle microflier performed best (the dispersal distance is 1.56 times to the release height). To further investigate performance differences, we released the saddle and hemisphere microfliers simultaneously from heights of 30 m, 40 m, and 50 m, and recorded their landing points (Supplementary Fig. 12, details see "Methods" section). The results showed that as the release height increased, the performance gap between the two types of microfliers narrowed, and the hemisphere samples even exceeded the dispersal distance of the saddle samples in some cases (Fig. 4e). Thus, we suggested that at low altitudes, the microflier has shorter exposure to crosswinds, while the added weight (23 mg) of the hemisphere negatively impacted the dispersal performance.

In analyzing the flight behaviors of saddle and hemisphere microfliers, we observed a significant difference in rotational speeds (Supplementary Movie 4 and Fig. 4f) with all 4 different angles, which partially explained the aforementioned flight performance differences. The data showed that the hemisphere microflier achieved a rotational speed of 112.5 r min^{-1}, which was ~2.1 times higher than that of the saddle microflier (52.92 r min^{-1}), demonstrating superior self-rotation capability. Both flight performances of the two microfliers aligned with the simulation results in Fig. 2c, d, where distinct travel distances and rotational speeds could be observed. Outdoor experimental results demonstrated that the continuous-shape-changing of saddle and hemisphere microfliers could effectively adjust the aerodynamic characteristics, thereby modifying their flight performances.

Flexible multifunctional circuit and outdoor monitoring tests

Achieving high robustness of solar-powered microfliers posed challenges due to power conversion efficiency[28,29] and fluctuating sunlight[30,31], integrating solar energy with supercapacitors (CAP) and low-dropout regulators (LDOs)

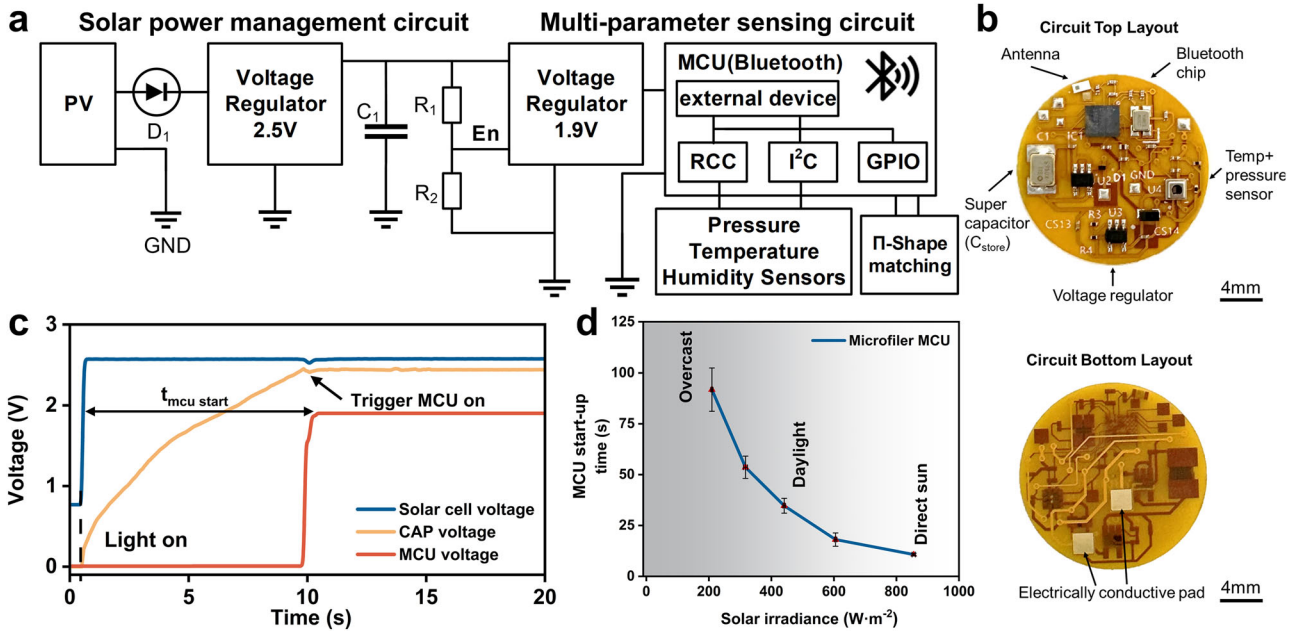


Fig. 5 | Flexible solar-powered wireless circuits. a Detailed diagram of the solar-powered flexible wireless circuits. **b** Top and bottom images show the layouts of solar-powered flexible wireless circuits. **c** Voltage waveforms of the solar cells, supercapacitors (CAP), and microcontroller unit (MCU) after the light turns on. This diagram illustrates that the MCU is successfully triggered after the CAP reaches the threshold voltage. **d** Time required to start the MCU under different light intensities (Error bars show standard deviation calculated from $N = 3$ independent trials).

offered a promising energy-harvesting solution for prolonging sensor operation duration in milligram-scale systems[14,18]. Based on this strategy, we designed a flexible solar-powered wireless circuit (Fig. 5a), which contained two main parts: the solar energy management module and the multi-parameter sensing module (details can be found in the "Methods" section). The entire circuit was integrated onto a flexible polyimide substrate with double-sided layouts to ensure the optimal aerodynamic structure (Fig. 5b). Active electronic components were positioned on the top surface to maintain a smooth lower aerodynamic profile. This design strategy ensured seamless integration with the biomimetic aerodynamic layer through the bottom surface.

Robust operation of the solar-powered microflier was achieved through the solar energy harvesting and management circuit module, alongside the integration of low-power functional devices (specific circuit selection details are provided in Supplementary Note 3). We measured the waveforms of the core components within the microflier during the start-up process (Fig. 5c). When the CAP voltage reached the 2.4 V threshold (at 10.42 s), the MCU activation sequence was initiated (≥1.6 V). Throughout the startup transient, the solar cell maintained a stable output of 2.57 V, ensuring consistent power delivery to the system through the charging and discharging characteristics of the CAP. Furthermore, we measure the start-up ability of the circuit at different light intensities (Supplementary Note 4), and the experimental results are shown in Fig. 5d. The results indicate that the MCU still successfully started after about 101.6 s of energy storage period at the light intensity of only ~206 W m^{-2}, demonstrating its excellent start-up ability even in low-light conditions. We also used linear regression ($R^2 \geq 0.98$) to generate a mapping between light intensities and throughputs of Bluetooth. The mapping results revealed that the developed microfliers could communicate at a rate of 0.1 packets every second with a lowest light intensity requirement of ~42.54 W m^{-2} after successfully starting up (as shown in Supplementary Fig. 13), showing robust communication capability of the proposed circuit. Thus, the designed multi-parameter sensing and wireless communication modules of the microflier could perform reliable operation across a wide range of light intensities.

In addition to evaluating the electrical performance of the prepared microflier in the lab conditions, we conducted detailed evaluation tests of the monitoring capabilities of microfliers in various outdoor environmental scenarios. Specifically, we tested the adaptive continuous-shape-changing and the self-sustained operation (both short-term and long-term) capabilities of resultant microfliers (see Supplementary Note 5 for details). The results showed an interesting phenomenon that under wind conditions (≥2.6 m s^{-1}), the saddle state microflier exhibited a "falling leaf" flight trajectory, while the hemisphere state microflier remained a stable flight trajectory (Fig. 6a and Supplementary Movie 5). Furthermore, the switch between the two flight trajectories could be achieved by controlling a single SMAA of the 2S-shape actuator unit. The deployment positions and operational statuses of microfliers are shown in Fig. 6b. Programming the adaptive characteristics of the microflier (e.g., temperature), the angles of microfliers were adaptively adjusted in response to environmental changes (from high θ to low θ). By calibrating the relationship between activation times and wing angles using on-board batteries (Supplementary Fig. 14a), we demonstrate distinct differences in dispersal distances across three configurations: the undeformed state (40°), the optimally deformed state (20°), and the over-deformed state (0°). The EAM was programmed with angle-specific activation times, and microfliers were deployed at 40 m in each of the three states under selected wind directions. Recorded dispersal distances averaged 53.75 m (40°), 61.06 m (20°), and 55.53 m (0°) for the saddle morphology and 58.01 m (40°), 65.65 m (20°), and 54.82 m (0°) for the hemisphere morphology, revealing superior dispersal performance at the 20° configuration (Supplementary Fig. 14b). This programmable angle-dispersion relationship enabled adaptive landing at designated monitoring sites by triggering shape changes in response to environmental sensing thresholds. But it was still necessary to select the wind direction before release to prevent the inherent unpredictability of wind direction.

To validate the short-term capability of microfliers, we selected 4 typical scenarios (forest, brushwood, hill, and road), in which environmental factors varied. The environmental parameter variations for each scenario were plotted (Fig. 6c), and the results showed that the microfliers adapted to diverse environments with their sensing systems starting reliably and continuous monitoring. To validate the long-term capability, the microflier was deployed on a sunlit lawn and transmitted data via Bluetooth after initialization. The microflier successfully recorded temperature and pressure variations over a week period (Fig. 6d, e and Supplementary Fig. 15). The devices consistently maintained a daily operational cycle, turned off at sunset, and successfully rebooted at sunrise. During days 4 and

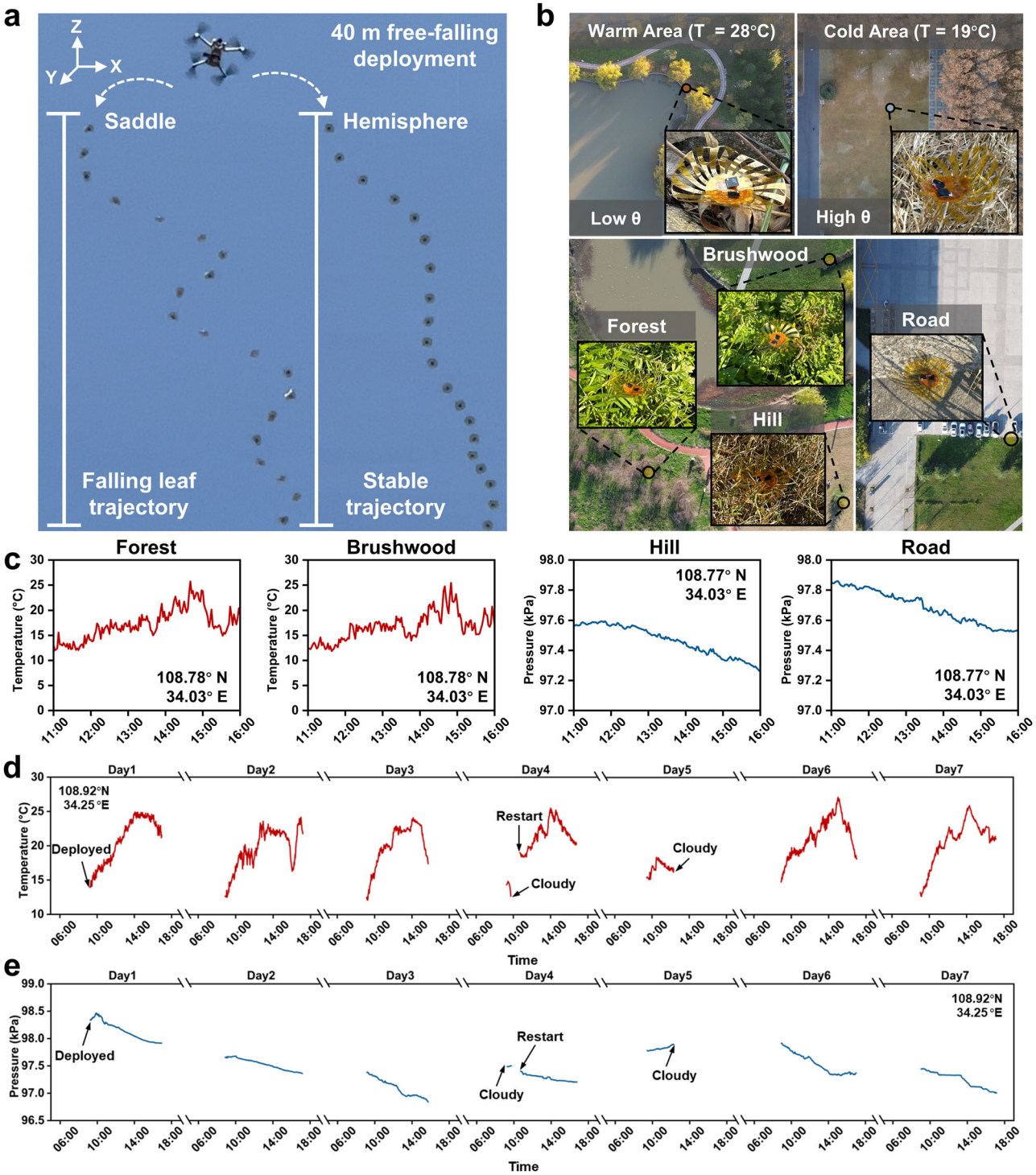


Fig. 6 | Outdoor environmental monitoring tests. a The flight trajectories of 40 m free-falling motion patterns of the saddle and hemisphere microfliers as observed in recorded test movies. **b** The landing positions and final states of the microfliers after dispersion in warm/cold areas and four typical environments (forest, brushwood, hill, and road). **c** The short-term monitoring data of different environmental parameters obtained by microfliers in 4 typical scenarios of (**b**). Variations of environmental parameters are measured in every 2 min. **d**, **e** Temperature and pressure readings from a 7-day outdoor deployed microflier.

5, intermittent shutdowns occurred due to persistent cloudy weather, with normal operation resumed promptly once light intensity levels recovered, demonstrating exceptional operational stability and system reliability under variable weather conditions. Temperature errors caused by self-heating effects were corrected (compensation factor $k = 0.8$), and the corrected temperature and pressure curves showed a deviation of less than 15.94% as compared to the reference data from National Meteorological Agency (Supplementary Fig. 16). Thus, the microfliers could adaptively continuously change their aerodynamic shapes in response to environmental changes and achieve robust long-term self-sustained operation after landing.

Discussion

In this study, we reported the adaptive continuous-shape-changing solar-powered microfliers with a minimal total weight of 198 mg, which could adjust the aerodynamics and achieve programmable flight performances

and ensure self-sustaining operation after deploying from a drone. The proposed design and fabrication strategy have addressed shape deformation limitations of existing microfliers[32,33] by developing adaptive abscission and continuous-shape-changing mechanisms to enhance intelligent programmable control of two basic aerodynamic shapes (saddle and hemisphere) for swarm adjusting wind dispersal, and developed a heterogeneous integration strategy to overcome extreme constraints (size, weight, and power) of microflier designs. Existing microfliers' actuators (such as electromagnetic actuators[18], piezoelectric actuators[34], dielectric elastomer actuators[35]) were known to possess large force output and fast response speed, which inevitably led to disturbed flight balance and extra weight. The proposed SMAAs demonstrated minimized impact on aerodynamic configurations during shape-changing processes due to their lightweight and simplified structure[36]. Meanwhile, the high programmability of SMAAs units presented substantial potential for engineering intelligent microfliers, which should be much desired for autonomous robotic platforms[37]. The adaptive continuous shape-changing mechanism was developed to regulate the flight behaviors of the microfliers under varying environmental conditions. Structural variations between individual microfliers (e.g., in initial humidity responsiveness) could induce subtle shape changes. This swarm regulation mechanism facilitated more uniform initial dispersal prior to encountering complex near-ground environments, thereby increasing coverage area. In proximity to the ground or within complex structures (e.g., vegetation, buildings), airflow patterns became highly variable and were influenced by localized factors. For microfliers tasked with sensing aerial environmental parameters, designs like the saddle structure were susceptible to deviating from intended paths or landing prematurely due to turbulence. Conversely, hemisphere microfliers exhibited enhanced residence capability. On this basis, the shape change enabled them to achieve enhanced suspension or controlled drift rather than passing rapidly through the target zone, within specific environmental parameters, gradient layers (e.g., the high-humidity gradient around a lake or the temperature gradient forests with fire hazards).

In addition, our microfliers were complete self-sustaining systems that integrated functional devices and offered great potential for large-scale[38] and intelligent deployment of sensor mesh networks[39–41]. The two distinct flight modes (saddle and hemisphere) enabled by the different SMAAs integration strategies further extended the wind dispersal potential of the microfliers. The stable flight performances of the hemisphere configuration could facilitate the wide area dispersal of microfliers, and the unpredictable flight trajectories of the saddle configuration might enable some novel applications, e.g., antipredator defense motion for many organisms[24]. Based on environmental wind speed, the microfliers could switch between the falling leaf trajectory and the stable trajectory. Thus, the proposed designs showed a high level of intelligent controls, and the research disclosed herein could open up a new avenue towards the development of bio-inspired microrobots for diverse intelligent applications. Meanwhile, the feasibility and cost of microfliers in large-scale manufacturing are high-value issues for engineering applications. We calculated the costs of each component of a microflier (Supplementary Table 2) to show the low manufacturing cost of the microfliers. The total cost for a single microflier was approximately $9.56. Microlfier used mature commercial electronic components, and the manufacturing process of Flexible Printed Circuit Board (FPCB) could also be extended to a large-scale process. This price, component selection, and preparation process were all capable of supporting the large-scale production application of the microfliers. This price, component selection, and preparation process are all capable of supporting the large-scale production application of our microfliers. But the large-scale production may inevitably lead to an environmental sustainability issue during its widespread use. Therefore, we propose the following three solutions to alleviate electronic pollution to a certain extent. We propose magnetic retrieval as a viable solution. By incorporating micro-scale ferrous elements into the microflier, these devices can be efficiently collected using magnetic sweepers. This approach, experimentally validated for feasibility[18], offers a practical pathway for large-scale recovery. To further mitigate the environmental footprint, the proposed design framework can be replaced with eco-friendly synthetic polymers (e.g., PLA and PHB). This material substitution can be directly implemented without compromising core functionality. The proposed microfliers can be extended by integrating biodegradable sensors and supercapacitors as well[42,43]. This evolution would effectively minimize long-term environmental persistence post-mission.

The novelty of this work lay in the following aspects: the designed microfliers mimic the adaptive abscission and continuous-shape-changing dispersal mechanisms of dandelion seeds and further enhance their adaptability from a single-environmental factor to multi-environmental factors; the SMAAs, together with EAM, enable adaptive continuous-shape-changing of microfliers, resulting in programmable aerodynamics and high flight performance; the proposed microfliers exhibited controlled interval deployments, multi-mode flight performances, and robust self-sustaining operations in ambient conditions. While our microflier designs demonstrate the ability of adaptive continuous-shape-changing to adjust the structural aerodynamics, real-time programmable shape-changing in response to environmental stimuli during flight will enable enhanced intelligent precision control of artificial microfliers. Furthermore, the power supply that enables the microfliers to continuously change shape still relies on EAM. Therefore, future research redirection of this system can be increasing the interaction ability between biomimetic aerodynamic structure and environment, reducing the energy consumption of the actuators, and further miniaturizing the size and weight of integrated electronic microcomponents.

Methods

Finite element simulations

We used programming and graphic design software (LibreCAD and Blender) to generate a structure consisting of arc-shaped pappi rotating around a central circle (20 mm in diameter). Specifically, 20 arc-shaped pappi were created, rotated at 18° intervals. The arc-shaped structures were designed based on the curvature of the samara seed edge (curvature $\rho \approx 0.042\ \mathrm{mm}^{-1}$) and incorporated features such as an outer stiffness ring (2 mm in diameter), resulting in a flat patterned 2D model. Bézier curves were used to construct models by defining the edges from the root of the pappi structure to the outer ring of the stiffness circle. The differences in the projected areas of the arc-shaped pappi were given due to different angles, which were crucial for the microflier performances. We simplified the 3D models by assuming the central circle remained fixed during the dynamic simulations.

The proposed computational domain was configured as a cube with dimensions of 100 mm × 100 mm × 100 mm and designated as the fluid domain under laminar flow conditions. Initial velocity components in all spatial directions (x, y, z) were prescribed as $0\ \mathrm{m\,s}^{-1}$. A velocity inlet boundary condition was imposed on the y-z planar surface, where the inflow direction was normal to the inlet plane with a time-dependent velocity profile defined as $1\ \mathrm{m\,s}^{-1}$. The opposing planar surface was configured as a pressure outlet boundary condition, maintaining a static pressure of 0 Pa. This configuration established a unidirectional flow field along the principal axis of the cuboid domain. The structural model was configured as a solid domain with user-defined material properties. Solid mechanics analyses were implemented with a fixed constraint applied to the basal surface of the structural model. This configuration enabled systematic observation of deformation characteristics and stress distributions resulting from transverse fluid flow loading on the models.

Based on the established models of microfliers, a cube domain was created. Through the difference set in Boolean transformation, the microflier model domain was subtracted from the cube domain to obtain the flow field domain. The steady-state wind speed was $5\ \mathrm{m\,s}^{-1}$. Layered inlet and outlet planes were set according to the requirements of side wind and up-down wind. Specifically, we set specific wind speeds in the "without angle" ($5\ \mathrm{m\,s}^{-1}$) and "with angle" ($1\ \mathrm{m\,s}^{-1}$) groups based on the actual situation in Supplementary Fig. 5.

Biomimetic aerodynamic layer design and fabrication

Based on the established 2D models (Fig. 2a and Supplementary Fig. 3), we used a laser micro-machining machine to fabricate various biomimetic aerodynamic structures on 25 μm polyimide substrates. Specifically, six structures (Supplementary Fig. 4a) were designed with three diameters (40 mm, 50 mm, and 60 mm) and two shapes (straight and arc). Additionally, electrically conductive apertures and SMAA integration vias were incorporated into the original biomimetic aerodynamic patterns to facilitate the integration process (Supplementary Fig. 7).

Flexible circuits layer design

The flexible circuits were designed with a double-layer layout. The top side of the circuits featured a programmable microcontroller with an onboard Bluetooth radio (nRF52832, Nordic Semiconductor), which read data from temperature and pressure sensors (BMP384, Bosch). We also integrated a micro-ceramic antenna (ANT016008LCS2442MA1, TDK) to enhance communication range and offer active control and wireless communication capabilities. Additionally, the integrated supercapacitor (CPM3225A, Seiko) and LDOs (TPS71719DCKR, TPS71725DCKR, TI) ensured efficient and stable use of solar energy, providing appropriate power to all electronic components. The bottom side was vertically interconnected with the GaAs solar cells of 5 mm × 5 mm to minimize electrical wiring. Furthermore, we applied high-temperature vacuum lamination to add insulating layers on both sides of the polyimide substrate to effectively protect the circuits from external contaminants (like moisture and dust), which was essential for the long-term stable operation of electronic devices in harsh environments.

SMAAs and EAM design and fabrication

The SMAAs with diverse shapes were fabricated by deforming SMAs with precision tweezers and a heating platform. Before processing, each SMA was heated at temperatures ≥ 60 °C to regain its original straight state through the shape memory effect. Following the natural cooling process to ambient temperature (~25 °C), the SMAs were manually shaped into the desired curvature using the same tweezers with specific bending parameters dictated by the pre-designed arc-shaped structures. To ensure optimal electrical interface with the EAM power terminals, both ends of the SMAs were soldered with minimal tin solder deposits, which were applied to facilitate reliable connections via 36 AWG (American Wire Gauge) copper wires.

EAM communicated with a Bluetooth microcontroller module and various common-use sensor modules (such as light, temperature, and humidity sensors) available on the market. It was integrated with a delay and a battery, which provided powerful scalability and rapid iteration capabilities. Specifically, we used a Bluetooth microcontroller module with multiple serial ports and programming capabilities as the foundation. Communication was established through AO/DO and DATA interfaces with the chosen light sensor module (5 mm light-dependent resistor) and temperature-humidity sensors module (DHT11). A Delay module was connected to one GPIO pin of the Bluetooth microcontroller to monitor high and low levels, while the battery (a 3.7 V Li-ion battery) was connected to the positive and negative terminals of the entire EAM. When the Bluetooth microcontroller detected a change in the environmental conditions programmed into the sensor, it would drive the delay module to activate the power supply to the SMAA and further drive the SMAA to induce adaptive continuous-shape-changing of the microfliers.

Microflier integration strategy

The integration strategy of the microflier will be described from top to bottom (Fig. 1d), with the top side facing the light source. The top side of the microflier consisted of two 5 mm × 5 mm GaAs solar cells (connected in series using 36 AWG wires). The middle section comprised two core layers: the biomimetic aerodynamic layer and the flexible circuits layer, with SMAAs (diameters of 0.3 mm) units positioned on the bottom. The solar cells directly provided power to the back power supply area of the flexible circuit layer through conductive vias on the biomimetic aerodynamic layer, which were vertically interconnected and securely soldered. The two core layers were bonded and fixed using CA glue. The SMAAs unit at the bottom could be integrated in various configurations (Fig. 2f). The SMAA should control two layers with different thicknesses to achieve continuous-shape-changing, which could potentially lead to shape-changing inconsistencies. This issue could be effectively addressed by designing different stress-relieved regions. We chose to attach a thick flexible circuit layer (75 μm) to a segment of SMAA to provide enough shape-changing force, and a thin biomimetic aerodynamic layer (25 μm) was only affixed to two holes to provide a smaller deformation force (Supplementary Fig. 7). The results indicated that the programmable continuous-shape-changing process of microfliers could be achieved as intended.

Adaptive continuous-shape-changing performance experiments

The solar simulator (Newport Oriel Sol3A) was employed to provide different light illuminations. By adjusting the light intensities, the adaptive continuous-shape-changing performances of microfliers were measured (Fig. 3d and Supplementary Movie 1). The EAM was positioned at the center of the simulator light spot and programmed to initiate adaptive continuous-shape-changing when the photosensitive sensor detected light intensities exceeding the threshold (≥600 lux), resulting in a decrease of the microflier angle from high to low. Furthermore, environmental temperature variations were introduced via a hot plate to evaluate the adaptive shape-changing capabilities of microfliers (Fig. 3e and Supplementary Movie 2). The system was programmed to trigger adaptive continuous-shape-changing when the temperature detected values reach or exceed 40 °C, thereby causing the microflier angle to decrease from high to low.

Outdoor dispersal performance experiments

To demonstrate the differences in the outdoor dispersal performances of the microfliers, we conducted dispersion experiments on a standard outdoor soccer field (105 m × 68 m) with a 4-m gap between sections of grass. Before the experiment, we positioned a hot-wire anemometer (405i, Testo) in the direction of the microflier flight with 2 m above the release point to measure the lateral wind speed at a rate of 1 Hz. The selection of the release point was determined by the wind direction on the day of the experiments to make sure that the microflier landed within the soccer field, thereby ensuring the accuracy of the data analyses. During the experiments, the microfliers were placed on a drone (DJI Mavic Mini) equipped with a remote trigger. Once the drone reached the designated height at the release point, it triggered the microfliers' dispersion. To mitigate the influence of different wind speeds on dispersal performances, we released the microfliers from each comparison group simultaneously in each trial. A top-down view of the soccer field map was used to record landing positions. Trials were conducted sequentially to facilitate data recording. Furthermore, after marking the landing points on the map, we measured the exact dispersal distances and plotted the data in chart form to analyze the landing patterns of different types of microfliers. This approach enabled us to visually and quantitatively assess the performance of each microflier under various wind conditions.

Data availability

All data needed to evaluate the conclusions in this paper are present in the paper and/or the Supplementary Information. Additional data and raw data are available upon request from the corresponding author.

Code availability

The code that supports the findings within this manuscript is available from the corresponding authors upon reasonable request.

Received: 14 May 2025; Accepted: 19 September 2025;
Published online: 11 November 2025

References

1. Pfeifer, R., Lungarella, M. & Iida, F. Self-organization, embodiment, and biologically inspired robotics. *Science* **318**, 1088–1093 (2007).
2. Kim, S., Laschi, C. & Trimmer, B. Soft robotics: a bioinspired evolution in robotics. *Trends Biotechnol.* **31**, 287–294 (2013).
3. Floreano, D. & Wood, R. J. Science, technology and the future of small autonomous drones. *Nature* **521**, 460–466 (2015).
4. Egan, P., Sinko, R., LeDuc, P. R. & Keten, S. The role of mechanics in biological and bio-inspired systems. *Nat. Commun.* **6**, 7418 (2015).
5. Yang, G.-Z. et al. The grand challenges of science robotics. *Sci. Rob.* **3**, eaar7650 (2018).
6. Baines, R., Fish, F., Bongard, J. & Kramer-Bottiglio, R. Robots that evolve on demand. *Nat. Rev. Mater.* **9**, 822–835 (2024).
7. Greene, D. F. The role of abscission in long-distance seed dispersal by the wind. *Ecology* **86**, 3105–3110 (2005).
8. Schuchovski, C., Meulia, T., Sant'Anna-Santos, B. F. & Fresnedo-Ramírez, J. Inflorescence development and floral organogenesis in Taraxacum kok-saghyz. *Plants* **9**, 1258 (2020).
9. Wang, L., Liu, G. & Li, S. Attaching of dandelion seeds: results from morphology/structure and abscission force/angle. *Bioinspired Biomim. Nanobiomaterials* **12**, 52–60 (2023).
10. Seale, M. et al. Dandelion pappus morphing is actuated by radially patterned material swelling. *Nat. Commun.* **13**, 2498 (2022).
11. Cummins, C. et al. A separated vortex ring underlies the flight of the dandelion. *Nature* **562**, 414–418 (2018).
12. Andersen, M. C. Diaspore morphology and seed dispersal in several wind-dispersed Asteraceae. *Am. J. Bot.* **80**, 487–492 (1993).
13. Casseau, V., De Croon, G., Izzo, D. & Pandolfi, C. Morphologic and aerodynamic considerations regarding the plumed seeds of Tragopogon pratensis and their implications for seed dispersal. *PLoS ONE* **10**, e0125040 (2015).
14. Iyer, V., Gaensbauer, H., Daniel, T. L. & Gollakota, S. Wind dispersal of battery-free wireless devices. *Nature* **603**, 427–433 (2022).
15. Chen, Y. et al. Light-driven dandelion-inspired microfliers. *Nat. Commun.* **14**, 3036 (2023).
16. Yang, J., Zhang, H., Berdin, A., Hu, W. & Zeng, H. Dandelion-inspired, wind-dispersed polymer-assembly controlled by light. *Adv. Sci.* **10**, 2206752 (2023).
17. Yan, W. et al. Self-sensing dandelion-inspired flying soft actuator with multi-stimuli response. *Adv. Mater. Technol.* **9**, 2400952 (2024).
18. Johnson, K. et al. Solar-powered shape-changing origami microfliers. *Sci. Rob.* **8**, eadg4276 (2023).
19. Zhang, T. & Elomaa, P. Development and evolution of the Asteraceae capitulum. *New Phytol* **242**, 33–48 (2024).
20. Hawkes, E. et al. Programmable matter by folding. *Proc. Natl. Acad. Sci.USA* **107**, 12441–12445 (2010).
21. Liang, X. et al. Soft self-healing robot driven by new micro two-way shape memory alloy spring. *Adv. Sci.* **11**, 2305163 (2024).
22. Kim, B. H. et al. Three-dimensional electronic microfliers inspired by wind-dispersed seeds. *Nature* **597**, 503–510 (2021).
23. Qin, L., Jian, Z., Xu, Y. & Ma, L. On the attitude stability of flying dandelion seeds. *Phys. Fluids* **35**, 081904 (2023).
24. Tan, M., Zhang, S., Stevens, M., Li, D. & Tan, E. J. Antipredator defences in motion: animals reduce predation risks by concealing or misleading motion signals. *Biol. Rev.* **99**, 778–796 (2024).
25. An, X., Cui, Y., Sun, H., Shao, Q. & Zhao, H. Active-cooling-in-the-loop controller design and implementation for an SMA-driven soft robotic tentacle. *IEEE Trans. Rob.* **39**, 2325–2341 (2023).
26. Yang, H., Xu, M., Li, W. & Zhang, S. Design and implementation of a soft robotic arm driven by SMA coils. *IEEE Trans. Ind. Electron.* **66**, 6108–6116 (2018).
27. Zhakypov, Z., Mori, K., Hosoda, K. & Paik, J. Designing minimal and scalable insect-inspired multi-locomotion millirobots. *Nature* **571**, 381–386 (2019).
28. Ye, T. et al. Localized electron density engineering for stabilized B-γ $CsSnI_3$-based perovskite solar cells with efficiencies >10%. *ACS Energy Lett.* **6**, 1480–1489 (2021).
29. Ye, T. et al. Ambient-air-stable lead-free $CsSnI_3$ solar cells with greater than 7.5% efficiency. *J. Am. Chem. Soc.* **143**, 4319–4328 (2021).
30. Wang, Z. et al. Flexible photovoltaic micro-power system enabled with a customized MPPT. *Appl. Energy* **367**, 123425 (2024).
31. Xu, J. et al. The state-of-the-art fundamentals and applications of micro-energy systems on-chip. *Natl. Sci. Open* **4**, 20240044 (2025).
32. Guo, K., Liu, M., Vella, D., Suresh, S. & Hsia, K. J. Dehydration-induced corrugated folding in *Rhapis excelsa* plant leaves. *Proc. Natl. Acad. Sci.USA* **121**, e2320259121 (2024).
33. Yang, M., Zhang, F. & Wang, S. Bioinspired strategies for biomimetic actuators from ultrafast to ultraslow. *Nano Res* **17**, 570–586 (2024).
34. Jafferis, N. T., Helbling, E. F., Karpelson, M. & Wood, R. J. Untethered flight of an insect-sized flapping-wing microscale aerial vehicle. *Nature* **570**, 491–495 (2019).
35. Chen, Y. et al. Controlled flight of a microrobot powered by soft artificial muscles. *Nature* **575**, 324–329 (2019).
36. Ogawa, Y., Ando, D., Sutou, Y. & Koike, J. A lightweight shape-memory magnesium alloy. *Science* **353**, 368–370 (2016).
37. Arabagi, V., Hines, L. & Sitti, M. Design and manufacturing of a controllable miniature flapping wing robotic platform. *Int. J. Rob. Res.* **31**, 785–800 (2012).
38. Alonso-Mora, J., Baker, S. & Rus, D. Multi-robot formation control and object transport in dynamic environments via constrained optimization. *Int. J. Rob. Res.* **36**, 1000–1021 (2017).
39. Jang, K.-I. et al. Self-assembled three dimensional network designs for soft electronics. *Nat. Commun.* **8**, 1–10 (2017).
40. Andreev, S., Dobre, C. & Misra, P. Internet of things and sensor networks. *IEEE Commun. Mag.* **58**, 74–74 (2020).
41. Xia, Q. et al. A state-of-the-art review of through-silicon vias: filling materials, filling processes, performance, and integration. *Adv. Eng. Mater.* **27**, 2401799 (2025).
42. Sethi, S. S., Kovac, M., Wiesemüller, F., Miriyev, A. & Boutry, C. M. Biodegradable sensors are ready to transform autonomous ecological monitoring. *Nat. Ecol. Evol.* **6**, 1245–1247 (2022).
43. Lee, H. et al. Facile fabrication of a fully biodegradable and stretchable serpentine-shaped wire supercapacitor. *Chem. Eng. J.* **366**, 62–71 (2019).

Acknowledgements

The authors acknowledge financial support from the Fundamental Research Funds for the Central Universities (D5000220072) and the Northwestern Polytechnical University (23GH0202211, 24SH0201254).

Author contributions

T. Ye conceived the research and designed the experiments. H. Sun designed the microfliers and conducted the mechanical and electrical experiments. C. Yang and Z. Wang conducted the finite element simulation experiments. Y. Wang and X. Zhang prepared the outdoor experiments. T. Ye, H. Sun, and C. Yang wrote the manuscript. Y. Ren and W. Li contributed to the analysis of the electrical and outdoor experimental data. H. Chang, K. Li, Y. Huang, B. Ma, and W. Yuan revised the manuscript.

Competing interests

The authors declare no competing interests.

Additional information

Supplementary information The online version contains supplementary material available at https://doi.org/10.1038/s44172-025-00516-0.

Correspondence and requests for materials should be addressed to Tao Ye.

Peer review information *Communications Engineering* thanks Xiuju Song and the other, anonymous, reviewers for their contribution to the peer review of this work. Primary Handling Editors: [Philip Coatsworth]. Peer review reports are available.

Reprints and permissions information is available at http://www.nature.com/reprints

Publisher's note Springer Nature remains neutral with regard to jurisdictional claims in published maps and institutional affiliations.

Open Access This article is licensed under a Creative Commons Attribution-NonCommercial-NoDerivatives 4.0 International License, which permits any non-commercial use, sharing, distribution and reproduction in any medium or format, as long as you give appropriate credit to the original author(s) and the source, provide a link to the Creative Commons licence, and indicate if you modified the licensed material. You do not have permission under this licence to share adapted material derived from this article or parts of it. The images or other third party material in this article are included in the article's Creative Commons licence, unless indicated otherwise in a credit line to the material. If material is not included in the article's Creative Commons licence and your intended use is not permitted by statutory regulation or exceeds the permitted use, you will need to obtain permission directly from the copyright holder. To view a copy of this licence, visit http://creativecommons.org/licenses/by-nc-nd/4.0/.

© The Author(s) 2025